APPLIED PHYSICS

Strongly enhanced and tunable photovoltaic effect in ferroelectric-paraelectric superlattices

Yeseul Yun[1,2], Lutz Mühlenbein[1,2], David S. Knoche[1,2], Andriy Lotnyk[3,4], Akash Bhatnagar[1,2]*

Ever since the first observation of a photovoltaic effect in ferroelectric $BaTiO_3$, studies have been devoted to analyze this effect, but only a few attempted to engineer an enhancement. In conjunction, the steep progress in thin-film fabrication has opened up a plethora of previously unexplored avenues to tune and enhance material properties via growth in the form of superlattices. In this work, we present a strategy wherein sandwiching a ferroelectric $BaTiO_3$ in between paraelectric $SrTiO_3$ and $CaTiO_3$ in a superlattice form results in a strong and tunable enhancement in photocurrent. Comparison with $BaTiO_3$ of similar thickness shows the photocurrent in the superlattice is 10^3 times higher, despite a nearly two-thirds reduction in the volume of $BaTiO_3$. The enhancement can be tuned by the periodicity of the superlattice, and persists under 1.5 AM irradiation. Systematic investigations highlight the critical role of large dielectric permittivity and lowered bandgap.

INTRODUCTION

Recently, there has been a huge surge in the interest surrounding ferroelectric-paraelectric superlattice structures (SLs) (*1*, *2*). Although the concept of SLs was first introduced in the seminal work of Esaki in 1974 (*3*) in the pursuit of quantum wells in alternating layer GaAs-AlAs SLs, these structures were first synthesized with a ferroelectric oxide, $BaTiO_3$ (BTO), by Tabata *et al.* (*4*) with $SrTiO_3$ (STO) as the other layer. The resultant structures evidently demonstrated much higher values of dielectric permittivity (ε_r) (*4*, *5*) and ferroelectric polarization (*6*, *7*). The underlying origin was analyzed in the work of Neaton and Rabe (*8*) using density functional theory (DFT), which attributed the enhanced effects to persistence of in-plane strain imposed by the mismatch with the substrate, and internal electric field associated with the SL that additionally polarizes neighboring STO layers, resulting in overall higher polarization. In another approach, involving an SL of $PbTiO_3$ (PTO) and STO layers, Landau theory (typically used for bulk ferroelectrics) was demonstrated to be rather effective in predicting the enhancement in polarization and overall ferroelectric character (*7*). However, in certain cases, the dielectric properties were also found to be governed by Maxwell-Wagner relations with the dielectric layers forming the capacitors and the in-between interface approximated as either conducting or semiconducting, albeit in low-frequency regime (*9*). Lately, PTO/STO SLs have also garnered immense attention from the scientific community due to the observation of complex topologies, such as polar vortices, and polar skyrmions, which are reminiscent of magnetic skyrmions (*2*). Another consequence of sandwiching thin ferroelectric layers between paraelectric layers is the destabilization of polarization, which was demonstrated to be instrumental in extracting negative capacitance (*1*).

The realms were further extended to a three-material superlattice, instead of a two-material superlattice, with the A-site position occupied by isovalent ions (namely, Ba^{2+}, Ca^{2+}, and Sr^{2+}) and Ti^{4+} at the B-site. Ab initio calculations were used to illustrate that the typical double-well potential of the ferroelectric becomes much more asymmetric (*10*). Subsequent experimental work involving SLs of ferroelectric BTO and centrosymmetric STO and $CaTiO_3$ (CTO) layers demonstrated enhanced polarization and much higher dielectric response (*11*). The outcome corroborated the theoretical predictions (*12*) and implied broken inversion symmetry along the thickness of the superlattices with potential contributions from off-centering of Ti^{4+} in neighboring STO and CTO layers. Alternatively, in a more recent work, pressure applied with a tip of an atomic force microscope has been demonstrated to be effective in breaking the local inversion symmetry in STO crystals (*13*). However, it will be rather ambitious to conceptualize scenarios wherein these tip-induced pressures can be practically used. Therefore, layered growth of oxides still appears to be the most promising pathway for tuning/breaking the inversion symmetry over a macroscale.

A critical consequence of a broken inversion symmetry is the bulk photovoltaic (BPV) effect. The effect is symmetry driven and fundamentally relevant in all ferroelectrics, including BTO. In conjunction, the systematic long-range ordering of ions associated with SLs, while the strain maintained, has been also proposed as a strategy to tune the bandgap (*14*). In the case of superlattices composed of $BiFeO_3$ (BFO) and $BiCrO_3$ layers, the interplay between the distortions of the octahedra, abrupt termination of polarization, and charge reconstruction at the interfaces were found to be critical in lowering the effective bandgap (*15*). As a result, the aforementioned structures present an exciting opportunity to investigate the impact of these different aspects on photocurrent generation.

In this work, we report a systematic investigation of photocurrent extracted from SLs consisting of BTO, STO, and CTO layers. Upon comparison with the response from a pure BTO layer, an surprising enhancement of three orders of magnitude is observed in the tricolor superlattice with light of energy of 3.06 eV and of around two orders of magnitude under solar irradiation. Comparison with two-color SL and temperature-dependent measurements highlight the necessity of the three-component system and rule out the contribution from interfaces. An analysis of the spectral photoresponse and dielectric measurements unravels the fundamental conditions to realize and engineer these drastic enhancements in PV current.

[1]Zentrum für Innovationskompetenz SiLi-nano, Martin-Luther-Universität Halle-Wittenberg, 06120 Halle, Germany. [2]Institute of Physics, Martin-Luther-Universität Halle-Wittenberg, 06120 Halle, Germany. [3]Leibniz Institute of Surface Engineering (IOM), 04318 Leipzig, Germany. [4]Laboratory of Infrared Materials and Devices, The Research Institute of Advanced Technologies, Ningbo University, 315211 Ningbo, China. *Corresponding author. Email: akash.bhatnagar@physik.uni-halle.de

RESULTS

Film Growth

All the samples investigated in this study were fabricated with a pulsed laser deposition (PLD) system equipped with an excimer laser of KrF (λ = 248 nm). The growth of the layers was monitored with reflection high-energy electron diffraction. The strain state of the samples was analyzed with x-ray diffraction, and in-depth structural characterization was conducted with a scanning transmission electron microscope (STEM). The samples were grown epitaxially on 0.5%Nb:STO (001) oriented substrates.

Henceforth, $(STO)_x/(BTO)_y/(CTO)_z$ superlattices with x, y, and z number of unit cells will be referred to as SBCxyz. The overall thickness for all the SLs discussed in this study was restricted to ≈200 nm, while the thickness of BTO was around 250 nm. All the SLs were terminated with two unit cells of STO at the top. A representative STEM image acquired from SBC222 shows individual layers of the materials and in-between interfaces (Fig. 1, A and B). Reciprocal space maps (RSMs) were measured around the (103) asymmetric plane to quantify the state of strain in the samples. In the case of pure BTO, the q_x value corresponding to the film is evidently different from that of the substrate, which implies minimal or no influence of the strain arising from the mismatch between the lattice parameters (Fig. 1C). This relaxation from the strain has been shown to be mediated via defect formation such as dislocations or nonstoichiometric deficiencies (*16*, *17*). Contrary to the BTO, RSMs from SBC555 (Fig. 1D) and SBC222 (Fig. 1F) reveal peaks that are aligned with that of the substrate indicating persistence of strain across the entire thickness. Similar results have been also reported in the case of BTO/STO SL, where the in-plane strain, imposed by each STO layer, largely suppresses the relaxation of the BTO layers (*4*, *5*). However, SBC252 (Fig. 1E) shows a partial strain relaxation of 1.02%, which is in agreement with a previous study that insisted that the strain is maintained only if the BTO thickness is smaller than the combined thickness of STO and CTO (*11*). In addition, SLs of SB55 and BC55 were also fabricated and the respective RSMs are provided in the Supplementary Materials (fig. S1).

Photoelectrical measurements

The photoelectrical measurements were conducted with laser illumination of energy of 3.06 eV (λ = 405 nm), with indium tin oxide (ITO) as the top transparent electrode. It is noteworthy to mention that although the optical bandgap of BTO has been reported in between 3.3 and 3.5 eV (*18*, *19*), light of energy of 3.06 eV has been successfully used to analyze the photoresponse (*20*). Vacancy- and point defect–related states within the bandgap apparently contribute to the generation of current upon illumination with sub-bandgap photon energies (*21*). Similar observations have also been reported in STO [bandgap between 3.2 and 3.6 eV (*18*)], where photon energies of 2.9 eV (*22*) and 3.06 eV (*13*) have been used to analyze the photoresponse.

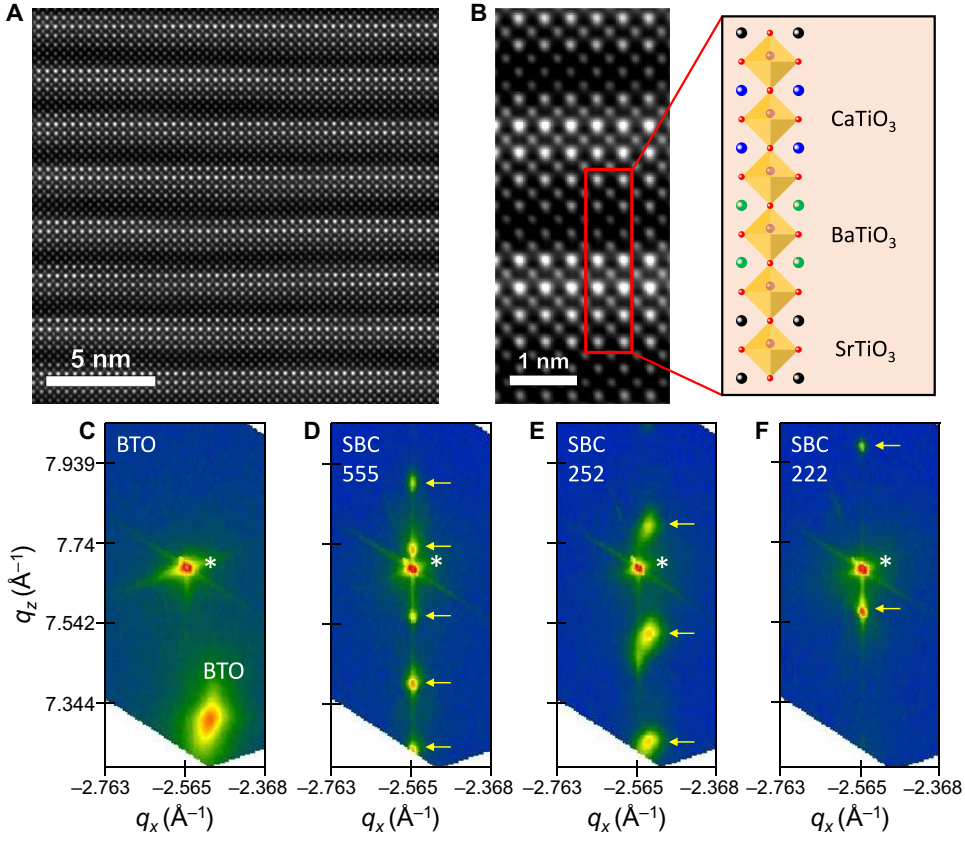

Fig. 1. Structural characterization of superlattices. (**A**) Cross-sectional STEM acquired from sample SBC222. (**B**) High-resolution STEM from a part of the scanned region. The schematic depicts the arrangement of unit cells. RSM acquired around (103) reflection in (**C**) BTO, (**D**) SBC555, (**E**) SBC252, and (**F**) SBC222. Star and yellow arrows indicate the STO substrate and satellite peaks from SL, respectively.

In Fig. 2 (A and B), current density-voltage (*IV*) and current-time measurements are presented, respectively. The *IV* characteristics were measured within the range of ±0.1 V to ensure that the samples are not subjected to any unintentional poling effects during the temperature-resolved measurements, which will be presented in subsequent sections. The chosen range of voltage inhibits any transient effects in the samples and allows reliable measurement of photocurrent, as has been also reported in previous studies (*23*). The photocurrent or the short-circuit current density (J_{SC}) extracted from BTO is around 0.415 μA/cm^2. Zenkevich *et al.* (*23*) reported nearly double J_{SC}, albeit with above bandgap illumination and thinner samples of around 50-nm thickness. Spanier *et al.* (*24*), in their work on BTO single crystals, achieved much higher J_{SC} (order of mA/cm^2) with 3.06 eV. The higher J_{SC} values were a consequence of novel tip-based geometry, which was found to be rather essential for the efficient collection of photo-generated carriers (*25*). The J_{SC} value from SBC555 is around 11.03 μA/cm^2 and is about 25 times higher than measured in BTO. The open-circuit voltage (V_{OC}) in the case of BTO was found to be around −0.007 V, as opposed to −0.058 V in SBC555. It must be emphasized here that BTO is the only material in this SL that is known and proven to exhibit a PV response. The PV characteristic of STO has only been recently unraveled (*13*) under extremely large strain gradients, while there are no reports on the observation of a PV effect in CTO. This makes it all the more intriguing that removal of nearly two-thirds of a PV material, and sandwiching the remaining one-third within an SL, results in such a high increment in photoresponse.

Synthesis in the form of SL architecture also inadvertently results in a higher number of interfaces. Depending upon the homogeneity and charge neutrality of the interface, photoelectronic contributions of residual character can be expected (*26*, *27*). To investigate the validity of such a scenario, two-color SLs consisting of STO/BTO (SB55) and BTO/CTO (BC55) were fabricated. Because the overall thickness of the samples was kept the same, the number of interfaces also remains the same. The J_{SC} values extracted from the linear fits for SB55 and BC55 are −0.331 and −0.128 μA/cm^2, respectively. As evident from Fig. 2A, while in the case of BC55 a reduction in BTO volume by half results in an obvious reduction in photocurrent, in the case of SB55 J_{SC} values similar to BTO are observed, albeit with opposite direction. It can be conjectured from this that BTO undergoes a flip in the polarization direction, which forces the direction of photocurrent to switch. This can be explained either due to the symmetry relations, that is, by the BPV effect (*28*, *29*), or via the reversal of the directionality of the diode formed at the electrode-ferroelectric interface (*30*). However, the response is still lower than SBC555. In conjunction, from Fig. 2B, the steady-state character of the photocurrent, along with abrupt rise and decay, is apparent. The absence of any residual effects, such as persistent photoconductivity (*27*), evidently suggests minimalistic role of interfaces in the overall photoelectronic process.

Temperature-resolved measurements

The *IV* characteristics of the samples were investigated across a temperature range of 77 to 293 K and are provided in fig. S2. The values of J_{SC} and V_{OC} extracted from linear fits are presented in Fig. 3, A and B, respectively. It is evident from Fig. 3A that the J_{SC} value from all the samples drops extensively as the temperature reduces to lower values. However, in the case of SB55, a rather interesting response is observed. The J_{SC} value not only undergoes a reversal in direction, being negative at room temperature and positive at lower temperature, but also continues to increase in magnitude until around 180 K. As a matter of fact, BC55 and BTO also exhibit, qualitatively, a similar response, albeit with much less magnitude, as visible from the inset of Fig. 3A. Curiously, BTO is known to undergo a phase transition from room temperature tetragonal phase to orthorhombic at around 273 K and to rhombohedral phase at around 183 K (*31*). The resemblance, in the range of temperature in which the prominent variations in J_{SC} occur with that of the phase transition in BTO, strongly suggests that the photoresponse measured in these samples is dominantly driven by the bulk symmetry of the material.

Another indication of a bulk-driven PV effect is the generation of an associated V_{OC} that is described by the overall conductivity of

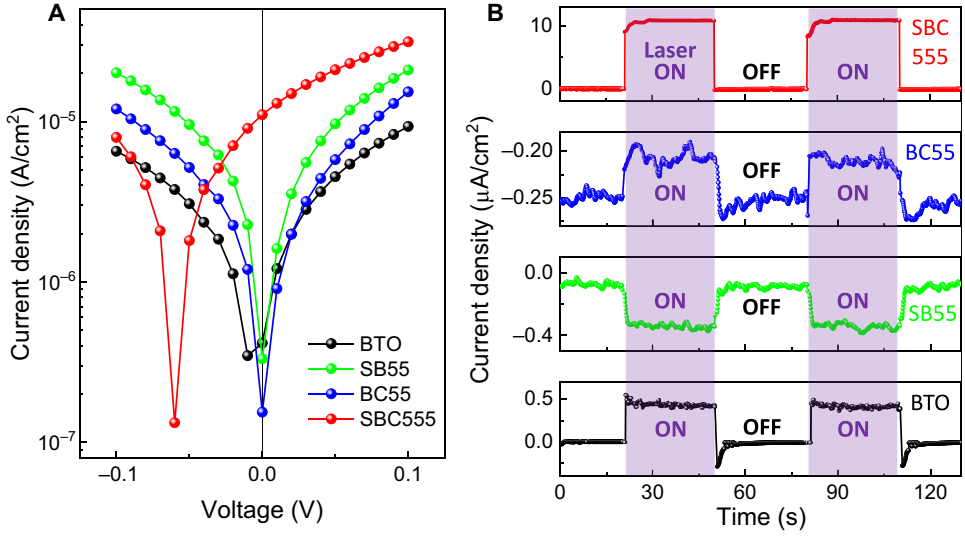

Fig. 2. Enhancement of photovoltaic effect in tricolor superlattices. (**A**) Current-voltage (*IV*) characteristics measured with 3.06 eV at room temperature. (**B**) Current-time response acquired with the illumination ON and OFF.

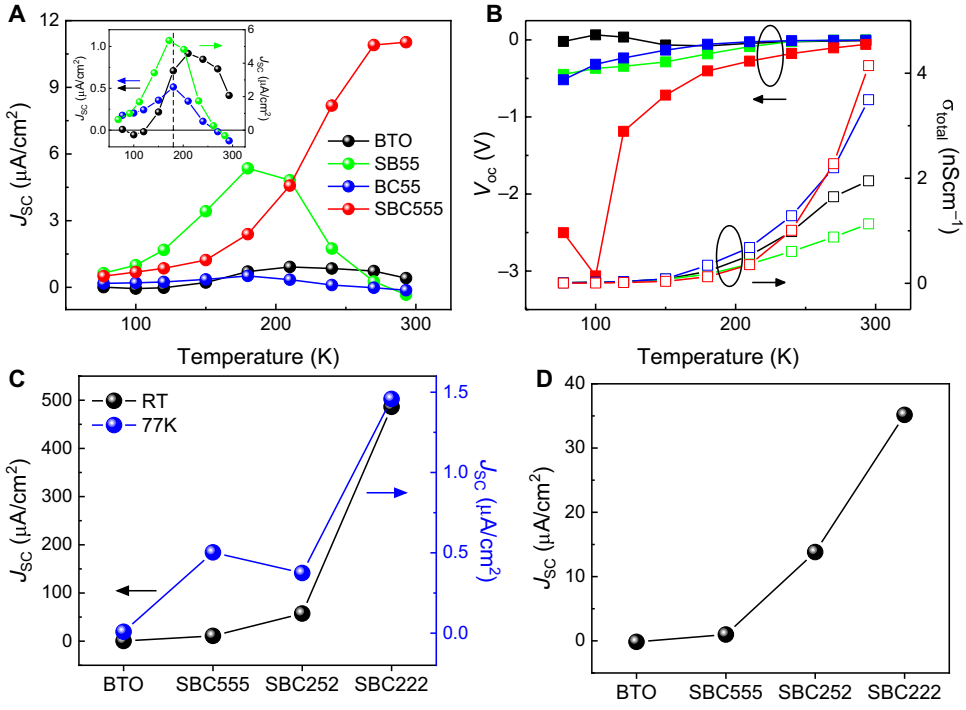

Fig. 3. Temperature- and periodicity-dependent photovoltaic effect. (**A**) J_{SC} extracted from *IV* characteristics acquired at different temperatures. The inset shows vertically magnified curves for BTO, SB55, and BC55. (**B**) Extracted values of V_{OC} and σ_{total} as a function of temperature. (**C**) J_{SC} measured in different samples at room temperature (RT) and 77 K. (**D**) J_{SC} measured under 1.5 AM solar illumination at room temperature.

the gap and is mathematically described with the following relation (*32*)

$$V_{OC} = \left(\frac{J_{SC}}{\sigma_d + \sigma_{ph}}\right) l \quad (1)$$

where σ_d and σ_{ph} are the dark conductivity and photoconductivity, respectively, and l is the distance between the electrodes. As evident from Fig. 3B, the measured V_{OC} values in all the samples drastically increase to higher values as the temperature lowers. The conformity with Eq. 1 was analyzed by measuring the associated σ_{total} (i.e., $\sigma_d + \sigma_{ph}$), which is also presented in Fig. 3B. It is clear that the conductivities drop exponentially in their respective magnitudes, which, following Eq. 1, results in higher V_{OC} values. In particular, SBC555 exhibits a V_{OC} value of around 3 V. This enhancement in V_{OC} upon lowering of temperature has also been observed in BFO exhibiting a BPV response (*33*). The massive reduction in the conductivities associated with the bulk and domain walls resulted in V_{OC} in excess of 20 V, albeit with much larger l of 50 μm. From these measurements, it becomes apparent that tricolor SLs consisting of SBC layers have an intriguing aspect that culminates in much higher photoresponse than two-color SLs or single layers.

To further investigate this, we synthesized variations of tricolor SL, namely, SBC252 and SBC222, with the same overall thickness as the other samples, i.e., 200 nm. The ferroelectric character of the SL was analyzed with piezo force microscopy, and a representative measurement indicating switching of polarization is presented in fig. S3. In Fig. 3C, J_{SC} values measured from the different tricolor SLs at room temperature are presented. The J_{SC} values were also found to be stable and consistent as a function of time (fig. S4). The role of symmetry in the observed PV response can be appreciated by the dependence of J_{SC} on the angle that the electric field of linearly polarized light makes with the direction of [010], as presented in fig. S5. Also noteworthy to mention is the reproducibility of the overall response that was found to be largely unchanged even over a period of 6 months (fig. S6). Apparently, this also rules out any transient character of the underlying origin. In comparison to BTO, a staggering enhancement of more than three orders of magnitude is observed in the case of SBC222, while an enhancement of 100 times is observed in SBC252. This trend persists even at lower temperature (Fig. 3C), although the magnitudes of J_{SC} in all the samples depreciate in values. A similar response was also observed under 1.5 AM solar illumination (Fig. 3D), with the difference between SBC222 and BTO at around 200 times. One of the possible reasons for such an enhancement in photocurrent could be a lowering of the bandgap.

Spectral photoresponse

The spectral photoresponse was acquired measuring the PV current as the wavelength of illumination was scanned from 700 to 320 nm (Fig. 4A). Because it is clear from Fig. 2A that the overall conductivities were rather high in the case of tricolor SLs at room temperature, the spectral response was measured at 77 K to circumvent any contribution from carrier effects and focus more on the intrinsic behavior (*9*). A striking similarity to the response previously measured (*28*) and predicted (*29*) in monodomain single crystals of BTO is observed. In addition, a distinct peak-like feature is visible at around 3.2 eV, which is generally accepted as the bandgap value of BTO. However, no such feature appears in the response acquired from any of the SL samples. Overall, the response in the SL remains higher than in BTO across all wavelengths. In particular, the response in SBC222 starts to rise at around 600 nm or 2.06 eV. This value is also

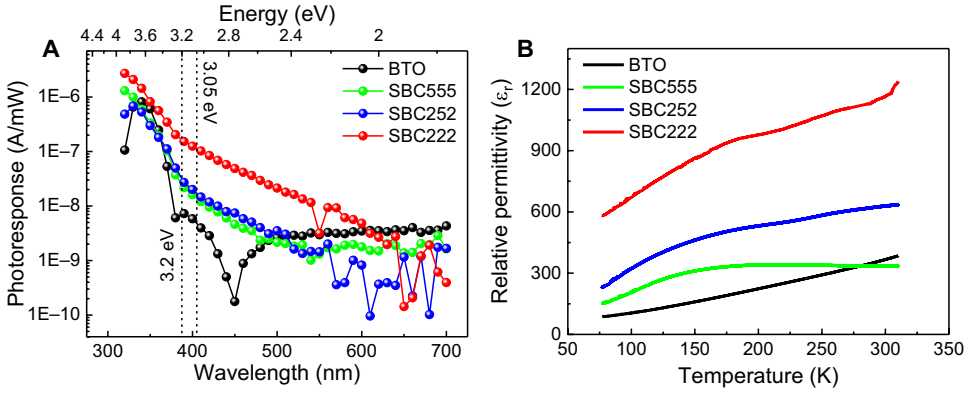

Fig. 4. Spectral photoresponse and dielectric characterization. (**A**) Spectral photoresponse measured at 77 K without any bias voltage. (**B**) Relative permittivity measured as a function of temperature with an ac signal of amplitude 100 mV and frequency 100 kHz.

in an striking agreement with the theoretical work based on DFT calculations, which predicted an indirect bandgap of 2.09 eV and a direct bandgap of 2.39 eV in an SBC superlattice, albeit consisting of only one unit cell of each material (*14*). This could also be the underlying origin for reduced J_{SC} in SBC222 at low temperatures, as the phonons needed for the in-direct band transition are sparse. A similar trend is also observed in SBC252 and SBC555, where the response initiates to rise at around 500 nm, which corresponds to 2.48 eV. The measurement therefore suggests a substantial lowering in the bandgap.

A similar lowering in the bandgap was calculated in a layered/superlattice system consisting of $PbNiO_2$ and PTO (*34*). An intricate coupling between a Ni-ion and an oxygen vacancy, repeated with a periodicity of 1 and 2 nm, at the B-site of the unit cell essentially pushed the bandgap down from ultraviolet to visible range. Another critical outcome of the layering was the delocalization of the conduction band minima accompanied with a larger magnitude of the shift current vector, eventually leading to higher photocurrents. The J_{SC} values were estimated to be around 43 times higher. The subtle displacements in the position of cations, arising from the layered arrangement (*12*, *34*), were found to be the driving factor. A similar scenario can also be perceived to be relevant for SLs presented in this study. Also noteworthy to mention is the case of $Bi(Fe_{0.5},Cr_{0.5})O_3$, where layering, achieved via a sequential arrangement of Fe and Cr-ions at the B-site, caused a substantial drop in the absorption energies from ≈2.7 to ≈1.5 eV (*35*). The resultant J_{SC} was measured to be enhanced by four times. Thus, it will be rather ambitious to attribute the large enhancement of J_{SC} observed in this work to only lowering of the bandgap. The samples were analyzed for their respective dielectric response to further our understanding on the complimentary effects at play.

Dielectric characterization

The dielectric characteristics were measured across the same range of temperature as the photoelectrical properties. A small ac signal of 100 mV at 100 kHz was used to record the dependence of the capacitance on the temperature from which the relative dielectric constant (ε_r) of the measurement gap was calculated (Fig. 4B). The high ac frequency allows to circumvent the probable contributions of free carriers and focus on the intrinsically related ε_r (*9*, *36*). At room temperature, BTO exhibits an ε_r value of around 355, which is comparable to the values reported in previous studies (*37*, *38*). The ε_r value of BTO steadily decays to lower values as the temperature approaches 77 K. Such a decay has also been observed in single crystalline (*39*) and polycrystalline (*40*) forms of BTO. This appears as an inherent characteristic that can be attributed to the thermal activation of domain wall mobility that lowers the ε_r and, in turn, the measured capacitance (*39*). The decrease in ε_r at lower temperatures is also observed in the SL and is largely congruent with previous studies involving SLs consisting of $LaAlO_3/Ba_{0.8}Sr_{0.2}TiO_3$ (*41*) and PTO/STO (*1*). However, the overall ε_r remains higher in SBC222 and SBC252 across the entire range of temperature.

The higher ε_r can be critical in those photoelectronic mechanisms that proceed via formation of excitons, i.e., generation of electron-hole pairs upon photon absorption. The binding energy of the exciton is dominantly influenced by Coulomb interaction energy, which is inversely proportional to ε_r of the medium. In the case of organic semiconductors, the PV effect was found to be enhanced by around 30% upon the modification of ε_r by ≈2.4 times (*42*). In this work, the ε value of SBC222 is around 3.2 times higher than that of BTO at room temperature and 6.7 times higher at 77 K. Interestingly, excitons have also been found to be rather prevalent in BTO (*43*) and other ABO_3-type perovskite systems (*44*, *45*), with experimental observations related to luminescence at low and room temperatures serving as proof (*46*, *47*).

DISCUSSION

The aforementioned results and corresponding analysis present an innovative strategy to extract a higher PV response from a ferroelectric material. The enhancement in photocurrent persists across a wide range of temperatures and over long periods of time, indicating the robustness and inherent character of the underlying origin. The comparison between two- and three-color SLs allows us to rule out the impact of any interfaces and highlights the importance of three-color SL. In conjunction, the periodicity was found to be a critical parameter in further improving the PV response, as much higher response was observed in SBC222 in comparison to SBC555. A similar strategy was also proposed and implemented to induce a compositional breaking of inversion symmetry in SLs consisting of ferroelectric material (*10*, *48*). As per current state of knowledge, the impact of this compositional control of inversion symmetry on the BPV effect, arising from shift mechanism (*29*), is not clear. Anyhow, in the samples investigated in this study, ε_r exhibited a rather

symmetric response to applied dc bias (fig. S7). Hence, there is no evidence of any prominent modulation in the compositional inversion symmetry. Another aspect to consider is the state of strain that massively influences the off-centering of B-site ion (Ti^{4+}) and tetragonality ratio. As a result, different studies have demonstrated the impact of strain on the photoresponse in ferroelectric oxides, via either bandgap modulation (*49*) or activity of sub-bandgap states (*50*). But in this study, SBC252, which is partially relaxed, evidently exhibits a much higher response than SBC555 that is completely strained. In addition, the photoresponse from SBC222 is 1000 times higher than that from BTO, although the tetragonality ratio in BTO is 1.02, while that in SBC222 is 1.01 (fig. S8). Therefore, it can be conjectured that strain does not appear to have a dominant role in the observed enhanced effects.

Nevertheless, ε_r of the SLs, in particular SBC222 and SBC252, was always found to be higher than that of bare BTO. Higher ε_r becomes a crucial parameter if exciton generation upon photon absorption is considered. A PV effect mediated by exciton generation and dissociation has also been observed in BFO thin films via transition optical absorption spectroscopy (*44*). Although the exciton might not traverse the distance between the electrodes, an encounter with a defect such as grain boundary, interface, or domain wall can be sufficient for their dissociation into free carriers contributing to the PV current. The higher ε_r can further lower the binding energy of the exciton, which facilitates dissociation. Concurrently, the spectral distribution acquired from the SLs depicts that the PV activity initiates at much lower energy than in bare BTO, which is also in agreement with the theoretical studies, and suggests a modified electronic structure. Therefore, it can be proposed here that the unison of these two rather discrete phenomena—higher permittivity and lowering of the bandgap owing to a modified electronic structure—culminates into an overall enhanced PV effect in SLs.

Although the aspect of the BPV effect, arising from asymmetric structure, cannot be disregarded, as illustrated by the scaling-up of V_{OC} upon suppression of conductivity. In addition, the angle-dependent J_{SC} further bolsters this scenario. The BPV effect is typically categorized into two mechanisms, i.e., shift and ballistic. The ballistic mechanism, driven by asymmetric scattering of photo-generated carriers, can be expected to be more under the influence of extrinsic factors such as interfaces and defects states (*51*, *52*). On the other hand, the shift mechanism is intricately related to the real shift of carriers upon excitation in the conduction band. The dominant role of shift mechanism can be inferred from the comparison presented in Fig. 2, where, despite the same number of interfaces in SBC555, BC55, and SB55, J_{SC} is the highest in SBC555. However, detailed studies will be needed to investigate the coexistence of excitonic effects and shift currents in the SL, as recently reported in BTO (*52*), to harness the true potential of these structures. Hence, SLs provide a fascinating platform where the permittivity and bandgap energies can be effectively modulated to engineer a suitable PV material.

MATERIALS AND METHODS

Thin-film growth

All the films investigated in this study were grown on 0.5% Nb-doped STO (100) substrates with a PLD system (SURFACE PLD Workstation) equipped with a KrF excimer laser. The samples were grown at a temperature of 700°C under a partial pressure of 0.015 mbar of O_2 and subsequently cooled under approximately 200 mbar of O_2. The targets were ablated with a laser energy of around 1 J/cm^2 and repetition rate of 5 Hz. All the SLs were capped with two unit cells of STO.

Device fabrication

The substrates served the purpose of the bottom electrode for all the (photo-)electrical measurements, and ITO was used as the top electrode (350 μm in diameter) for photoelectrical characterization. Standard photolithography processes were used to design and pattern the electrodes. ITO was deposited with PLD under 0.02 mbar of O_2 partial pressure at room temperature with a laser energy of around 1 J/cm^2 and repetition rate of 10 Hz. Dielectric measurements were conducted with Cr/Au as the top electrodes (75 μm by 75 μm), which were deposited with e-beam evaporation. The thickness of ITO and Cr/Au electrodes is 80 nm and 100 nm, respectively.

Electrical measurements

The dc (photo-)electrical measurements were conducted with a high impedance electrometer (Keithley 6517B). The samples were illuminated with light from 405-nm laser (Cobolt 06 MLD) at 20-mW power and solar irradiation (1.5 AM). Temperature-dependent measurements were conducted in a cryostat from JANIS, connected to a temperature controller (Lakeshore 335). The spectral photoresponse was acquired upon illumination from a tunable monochromatic light source (BENTHAM TLS120Xe). The recorded values of photocurrent at each wavelength were normalized with the respective light intensity (A/mW). The dielectric measurements were conducted with an impedance LCR meter (Keysight E4980A). An ac signal of amplitude 100 mV and frequency 100 kHz was used.

Investigations with TEM

Cross-sectional specimens for TEM investigations were prepared by a combination of focused Ga high-energy (Zeiss Auriga Dual-beam FIB) and Ar low-energy ion beam milling (Fischione NanoMill). TEM studies were performed with a probe Cs-corrected Titan3 G2 60-300 microscope operating at 300 kV accelerating. The microscope is equipped with high-brightness gun (X-FEG), various annual detectors (Fischione, FEI), and Super-X energy-dispersive x-ray spectroscopy (EDS) system (FEI ChemiSTEM technology). Probe-forming aperture of 20 mrad was applied during STEM experiments. STEM images were recorded with an annular dark-field detector (Fischione) using annular ranges of 80 to 200 mrad. The detector ranges fulfill the condition corresponding to high-angle annular dark-field (HAADF) imaging or Z contrast imaging well. Hence, the atomic columns with higher average Z number in HAADF images appear brighter than those elements with lower average Z number. The C5 parameter was adjusted by the manufacturer to be 0.4 mm. Electron beam current measured on TEM specimen surface was set to a value of approximately 130 pA. The STEM images presented in this work were postprocessed by Wiener difference filter for the reduction of scanning noise and for enhancement of image intensity of individual atomic columns.

The lattice distances of BTO and SLs were estimated from atomic-resolution STEM-HAADF images. For the analysis, the HAADF images were acquired by using a rapid scanning of electron beam in STEM mode with a dwell time of 0.34 μs/pixel and with a sampling of 24 pm/pixel. For a STEM image with a size of 1024 pixels by 1024 pixels, this corresponds to 0.36 s per frame. A total number of 30 images were recorded to correct the stage drift and scanning distortions. The

corrections were done using rigid and nonrigid registration approaches implemented in the Smart Align software (HREM Research Inc.). The correction of residual image distortions was performed using the Jitterbug software (HREM Research Inc.). The STO substrate was used as the reference for the complete restoration of crystal lattice angles and lengths. Quantitative analysis of lattice distances in the studied structures was performed by detailed peak fitting using Peak Pairs Analysis software (HREM Research Inc.). The applied procedure allows measurements of interatomic distances with very high precision of several picometers.

SUPPLEMENTARY MATERIALS

Supplementary material for this article is available at http://advances.sciencemag.org/cgi/content/full/7/23/eabe4206/DC1

REFERENCES AND NOTES

1. P. Zubko, J. C. Wojdeł, M. Hadjimichael, S. Fernandez-Pena, A. Sené, I. Luk'yanchuk, J.-M. Triscone, J. Íñiguez, Negative capacitance in multidomain ferroelectric superlattices. *Nature* **534**, 524–528 (2016).
2. S. Das, Y. L. Tang, Z. Hong, M. A. P. Gonçalves, M. R. McCarter, C. Klewe, K. X. Nguyen, F. Gómez-Ortiz, P. Shafer, E. Arenholz, V. A. Stoica, S.-L. Hsu, B. Wang, C. Ophus, J. F. Liu, C. T. Nelson, S. Saremi, B. Prasad, A. B. Mei, D. G. Schlom, J. Íñiguez, P. García-Fernández, D. A. Muller, L. Q. Chen, J. Junquera, L. W. Martin, R. Ramesh, Observation of room-temperature polar skyrmions. *Nature* **568**, 368–372 (2019).
3. L. Esaki, L. L. Chang, New transport phenomenon in a semiconductor "Superlattice". *Phys. Rev. Lett.* **33**, 495–498 (1974).
4. H. Tabata, H. Tanaka, T. Kawai, Formation of artificial $BaTiO_3/SrTiO_3$ superlattices using pulsed laser deposition and their dielectric properties. *Appl. Phys. Lett.* **65**, 1970–1972 (1994).
5. O. Nakagawara, T. Shimuta, T. Makino, S. Arai, H. Tabata, T. Kawai, Epitaxial growth and dielectric properties of (111) oriented $BaTiO_3/SrTiO_3$ superlattices by pulsed-laser deposition. *Appl. Phys. Lett.* **77**, 3257–3259 (2000).
6. T. Shimuta, O. Nakagawara, T. Makino, S. Arai, H. Tabata, T. Kawai, Enhancement of remanent polarization in epitaxial $BaTiO_3/SrTiO_3$ superlattices with "asymmetric" structure. *J. Appl. Phys.* **91**, 2290–2294 (2002).
7. M. Dawber, N. Stucki, C. Lichtensteiger, S. Gariglio, P. Ghosez, J.-M. Triscone, Tailoring the properties of artificially layered ferroelectric superlattices. *Adv. Mater.* **19**, 4153–4159 (2007).
8. J. B. Neaton, K. M. Rabe, Theory of polarization enhancement in epitaxial $BaTiO_3/SrTiO_3$ superlattices. *Appl. Phys. Lett.* **82**, 1586–1588 (2003).
9. G. Catalan, D. O'Neill, R. M. Bowman, J. M. Gregg, Relaxor features in ferroelectric superlattices: A Maxwell–Wagner approach. *Appl. Phys. Lett.* **77**, 3078–3080 (2000).
10. N. Sai, B. Meyer, D. Vanderbilt, Compositional inversion symmetry breaking in ferroelectric perovskites. *Phys. Rev. Lett.* **84**, 5636–5639 (2000).
11. H. N. Lee, H. M. Christen, M. F. Chisholm, C. M. Rouleau, D. H. Lowndes, Strong polarization enhancement in asymmetric three-component ferroelectric superlattices. *Nature* **433**, 395–399 (2005).
12. S. M. Nakhmanson, K. M. Rabe, D. Vanderbilt, Polarization enhancement in two- and three-component ferroelectric superlattices. *Appl. Phys. Lett.* **87**, 102906 (2005).
13. M.-M. Yang, D. J. Kim, M. Alexe, Flexo-photovoltaic effect. *Science* **360**, 904–907 (2018).
14. B. Luo, X. Wang, E. Tian, G. Li, L. Li, Electronic structure, optical and dielectric properties of $BaTiO_3/CaTiO_3/SrTiO_3$ ferroelectric superlattices from first-principles calculations. *J. Mater. Chem. C* **3**, 8625–8633 (2015).
15. S. Zhang, H. Xiao, S. Peng, G. Yang, Z. Liu, X. Zu, S. Li, D. Singh, L. Martin, L. Qiao, Band-gap reduction in $(BiCrO_3)_m/(BiFeO_3)_n$ superlattices: Designing low-band-gap ferroelectrics. *Phys. Rev. Appl.* **10**, 044004 (2018).
16. Y. B. Chen, H. P. Sun, M. B. Katz, X. Q. Pan, K. J. Choi, H. W. Jang, C. B. Eom, Interface structure and strain relaxation in $BaTiO_3$ thin films grown on $GdScO_3$ and $DyScO_3$ substrates with buried coherent $SrRuO_3$ layer. *Appl. Phys. Lett.* **91**, 252906 (2007).
17. J. Q. He, E. Vasco, R. Dittmann, R. H. Wang, Growth dynamics and strain relaxation mechanisms in $BaTiO_3$ pulsed laser deposited on $SrRuO_3/SrTiO_3$. *Phys. Rev. B* **73**, 125413 (2006).
18. S. Piskunov, E. Heifets, R. Eglitis, G. Borstel, Bulk properties and electronic structure of $SrTiO_3$, $BaTiO_3$, $PbTiO_3$ perovskites: An ab initio HF/DFT study. *Comput. Mater. Sci.* **29**, 165–178 (2004).
19. S. H. Wemple, Polarization fluctuations and the optical-absorption edge in $BaTiO_3$. *Phys. Rev. B* **2**, 2679–2689 (1970).
20. F. Liu, I. Fina, D. Gutiérrez, G. Radaelli, R. Bertacco, J. Fontcuberta, Selecting steady and transient photocurrent response in $BaTiO_3$ films. *Adv. Electron. Mater.* **1**, 1500171 (2015).
21. V. V. Laguta, A. M. Slipenyuk, I. P. Bykov, M. D. Glinchuk, M. Maglione, D. Michau, J. Rosa, L. Jastrabik, Electron spin resonance investigation of oxygen-vacancy-related defects in $BaTiO_3$ thin films. *Appl. Phys. Lett.* **87**, 022903 (2005).
22. M. C. Tarun, F. A. Selim, M. D. McCluskey, Persistent photoconductivity in strontium titanate. *Phys. Rev. Lett.* **111**, 187403 (2013).
23. A. Zenkevich, Y. Matveyev, K. Maksimova, R. Gaynutdinov, A. Tolstikhina, V. Fridkin, Giant bulk photovoltaic effect in thin ferroelectric $BaTiO_3$ films. *Phys. Rev. B* **90**, 161409 (2014).
24. J. E. Spanier, V. M. Fridkin, A. M. Rappe, A. R. Akbashev, A. Polemi, Y. Qi, Z. Gu, S. M. Young, C. J. Hawley, D. Imbrenda, G. Xiao, A. L. Bennett-Jackson, C. L. Johnson, Power conversion efficiency exceeding the Shockley–Queisser limit in a ferroelectric insulator. *Nat. Photonics* **10**, 611–616 (2016).
25. M. Alexe, D. Hesse, Tip-enhanced photovoltaic effects in bismuth ferrite. *Nat. Commun.* **2**, 256 (2011).
26. H. Liang, L. Cheng, X. Zhai, N. Pan, H. Guo, J. Zhao, H. Zhang, L. Li, X. Zhang, X. Wang, C. Zeng, Z. Zhang, J. G. Hou, Giant photovoltaic effects driven by residual polar field within unit-cell-scale $LaAlO_3$ films on $SrTiO_3$. *Sci. Rep.* **3**, 1975 (2013).
27. A. Tebano, E. Fabbri, D. Pergolesi, G. Balestrino, E. Traversa, Room-temperature giant persistent photoconductivity in $SrTiO_3/LaAlO_3$ heterostructures. *ACS Nano* **6**, 1278–1283 (2012).
28. W. T. H. Koch, R. Munser, W. Ruppel, P. Würfel, Anomalous photovoltage in $BaTiO_3$. *Ferroelectrics* **13**, 305–307 (1976).
29. S. M. Young, A. M. Rappe, First principles calculation of the shift current photovoltaic effect in ferroelectrics. *Phys. Rev. Lett.* **109**, 116601 (2012).
30. L. Pintilie, I. Vrejoiu, G. L. Rhun, M. Alexe, Short-circuit photocurrent in epitaxial lead zirconate-titanate thin films. *J. Appl. Phys.* **101**, 064109 (2007).
31. M. Acosta, N. Novak, V. Rojas, S. Patel, R. Vaish, J. Koruza, G. A. Rossetti, J. Rödel, $BaTiO_3$-based piezoelectrics: Fundamentals, current status, and perspectives. *Appl. Phys. Rev.* **4**, 041305 (2017).
32. V. M. Fridkin, *Photoferroelectrics* (Springer, 1979).
33. A. Bhatnagar, A. Roy Chaudhuri, Y. Heon Kim, D. Hesse, M. Alexe, Role of domain walls in the abnormal photovoltaic effect in $BiFeO_3$. *Nat. Commun.* **4**, 2835 (2013).
34. F. Wang, S. M. Young, F. Zheng, I. Grinberg, A. M. Rappe, Substantial bulk photovoltaic effect enhancement via nanolayering. *Nat. Commun.* **7**, 13981 (2016).
35. R. Nechache, C. Harnagea, S. Li, L. Cardenas, W. Huang, J. Chakrabartty, F. Rosei, Bandgap tuning of multiferroic oxide solar cells. *Nat. Photonics* **9**, 61–67 (2015).
36. D. O'Neill, R. M. Bowman, J. M. Gregg, Dielectric enhancement and Maxwell–Wagner effects in ferroelectric superlattice structures. *Appl. Phys. Lett.* **77**, 1520–1522 (2000).
37. D. J. R. Appleby, N. K. Ponon, K. S. K. Kwa, S. Ganti, U. Hannemann, P. K. Petrov, N. M. Alford, A. O'Neill, Ferroelectric properties in thin film barium titanate grown using pulsed laser deposition. *J. Appl. Phys.* **116**, 124105 (2014).
38. Y. Yoneda, H. Kasatani, H. Terauchi, Y. Yano, T. Terashima, Y. Bando, Ferroelectric phase transition in $BaTiO_3$ films. *J. Cryst. Growth* **150**, 1090–1093 (1995).
39. O. Trithaveesak, J. Schubert, C. Buchal, Ferroelectric properties of epitaxial $BaTiO_3$ thin films and heterostructures on different substrates. *J. Appl. Phys.* **98**, 114101 (2005).
40. R. Thomas, V. K. Varadan, S. Komarneni, D. C. Dube, Diffuse phase transitions, electrical conduction, and low temperature dielectric properties of sol–gel derived ferroelectric barium titanate thin films. *J. Appl. Phys.* **90**, 1480–1488 (2001).
41. W. Gao, A. Khan, X. Marti, C. Nelson, C. Serrao, J. Ravichandran, R. Ramesh, S. Salahuddin, Room-temperature negative capacitance in a ferroelectric–dielectric superlattice heterostructure. *Nano Lett.* **14**, 5814–5819 (2014).
42. S. Y. Leblebici, T. L. Chen, P. Olalde-Velasco, W. Yang, B. Ma, Reducing exciton binding energy by increasing thin film permittivity: An effective approach to enhance exciton separation efficiency in organic solar cells. *ACS Appl. Mater. Interfaces* **5**, 10105–10110 (2013).
43. L. M. Prócel, F. Tipán, A. Stashans, Mott-wannier excitons in the tetragonal $BaTiO_3$ lattice. *Int. J. Quantum Chem.* **91**, 586–590 (2002).
44. Y. Li, C. Adamo, C. E. Rowland, R. D. Schaller, D. G. Schlom, D. A. Walko, Nanoscale excitonic photovoltaic mechanism in ferroelectric $BiFeO_3$ thin films. *APL Mater.* **6**, 084905 (2018).
45. M. L. Moreira, M. F. C. Gurgel, G. P. Mambrini, E. R. Leite, P. S. Pizani, J. A. Varela, E. Longo, Photoluminescence of barium titanate and barium zirconate in multilayer disordered thin films at room temperature. *J. Phys. Chem. A* **112**, 8938–8942 (2008).
46. E. Orhan, J. A. Varela, A. Zenatti, M. F. C. Gurgel, F. M. Pontes, E. R. Leite, E. Longo, P. S. Pizani, A. Beltràn, J. Andrès, Room-temperature photoluminescence of $BaTiO_3$: Joint experimental and theoretical study. *Phys. Rev. B* **71**, 085113 (2005).
47. E. R. Leite, L. P. S. Santos, N. L. V. Carreño, E. Longo, C. A. Paskocimas, J. A. Varela, F. Lanciotti, C. E. M. Campos, P. S. Pizani, Photoluminescence of nanostructured $PbTiO_3$ processed by high-energy mechanical milling. *Appl. Phys. Lett.* **78**, 2148–2150 (2001).
48. M. P. Warusawithana, E. V. Colla, J. N. Eckstein, M. B. Weissman, Artificial dielectric superlattices with broken inversion symmetry. *Phys. Rev. Lett.* **90**, 036802 (2003).

49. F. Wang, I. Grinberg, A. M. Rappe, Band gap engineering strategy via polarization rotation in perovskite ferroelectrics. *Appl. Phys. Lett.* **104**, 152903 (2014).
50. A. Bhatnagar, Y. H. Kim, D. Hesse, M. Alexe, Persistent photoconductivity in strained epitaxial $BiFeO_3$ thin films. *Nano Lett.* **14**, 5224–5228 (2014).
51. G. Dalba, Y. Soldo, F. Rocca, V. M. Fridkin, P. Sainctavit, Giant bulk photovoltaic effect under linearly polarized x-ray synchrotron radiation. *Phys. Rev. Lett.* **74**, 988–991 (1995).
52. R. Fei, L. Z. Tan, A. M. Rappe, Shift-current bulk photovoltaic effect influenced by quasiparticle and exciton. *Phys. Rev. B* **101**, 045104 (2020).

Acknowledgments: We thank K. Dörr and D. Rata for x-ray measurements, M. Lisca for technical support, B. Fuhrmann and S. Schlenker for support with the facilities at the Interdisziplinäre Zentrum für Materialwissenschaften (IZM), and D. Hesse for carefully reading this manuscript. We are thankful to Fraunhofer Center for Silicon Photovoltaics (Halle) for the use of solar simulator. **Funding:** This study was supported by Bundesministerium für Bildung und Forschung (BMBF) Project No. 03Z22HN12, Deutsche Forschungsgemeinschaft (DFG) within Sonderforschungsbereiche (SFB) 762 (project A12), and Europäischen Fonds für regionale Entwicklung (EFRE) Sachsen-Anhalt. **Author contributions:** A.B. conceptualized and supervised the project. A.B. and Y.Y. designed the experiments and co-wrote the manuscript. Y.Y. was responsible for thin-film growth, photoelectrical measurements, and structural analysis. L.M. and D.S.K. contributed with device fabrication and configuration of photoelectrical setup. A.L. performed TEM-related experiments and analyzed the data. All the authors provided their inputs for the manuscript. **Competing interests:** The authors declare that they have no competing interests. **Data and materials availability:** All data needed to evaluate the conclusions in the paper are present in the paper and/or the Supplementary Materials.

Submitted 20 August 2020
Accepted 15 April 2021
Published 2 June 2021
10.1126/sciadv.abe4206

Citation: Y. Yun, L. Mühlenbein, D. S. Knoche, A. Lotnyk, A. Bhatnagar, Strongly enhanced and tunable photovoltaic effect in ferroelectric-paraelectric superlattices. *Sci. Adv.* **7**, eabe4206 (2021).